ACI STRUCTURAL JOURNAL TECHNICAL PAPER

Title No. 118-S44

Influence of Spatial Variability of Concrete in Large Shear-Critical Structures

by Mark D. Hunter, Anca C. Ferche, and Frank J. Vecchio

The implications of the spatial variability of concrete mechanical properties on the numerical analysis of a slab strip specimen (PLS4000) with no shear reinforcement are investigated. The 4.0 m (13 ft) thick specimen was tested by Collins et al. Hunter undertook a subsidiary experimental program to assess the spatial variability of the concrete through ultrasonic pulse velocity measurements taken on the PLS4000 specimen. The spatial variability was then included in finite element analyses of the specimen using stochastic methods. It was found that the spatial variability of the concrete mechanical properties influenced the crack pattern and development of the critical failure crack.

Keywords: finite element analysis; reinforced concrete; spatial variability; ultrasonic pulse velocity.

INTRODUCTION

Reinforced concrete structures in the field typically exhibit relatively large variations in the mechanical properties of the in-place concrete, stemming mainly from batch-to-batch variations, differences in concrete placement and curing practices, and inherent heterogeneity of the concrete matrix.[1-3] Depending on the type of the structure, reinforcement configuration, and load-carrying mechanism, this spatial variability of the concrete mechanical properties can potentially have a notable impact on the overall behavior and failure mode. It may be particularly influential to the performance of large shear-critical structures containing little or no shear reinforcement, for example, deep slabs or wind turbine foundations.

Research on spatial variability in the context of reinforced concrete structures has been mostly centered on the calculation of structural reliability and structural fragility with a focus on the effects of deterioration due to corrosion of the reinforcement bars.[4,5] However, the behavior of large concrete members containing reduced reinforcement ratios is highly dependent on the behavior of the concrete and thus on its mechanical properties.

This paper investigates the effect that spatial variability of concrete strength can have on the calculated response of a large slab strip specimen, PLS4000, tested at the University of Toronto by Collins et al.[6] and Quach.[7] In a related study, conducted by Hunter,[8] ultrasonic pulse velocity (UPV) measurements were taken from a grid of points on PLS4000, prior to its testing, to assess the spatial variability of the concrete component. The spatial variability was then incorporated into nonlinear finite element modeling, using stochastic methods. The results, discussed herein, provide an indication of the confidence one should have in regards to the calculated strength of large shear-critical structures containing little or no shear reinforcement.

RESEARCH SIGNIFICANCE

Concrete structures are designed and analyzed as homogenous monolithic structures at the structure level and at the member level. For small members, all cast from the same batch of concrete, this is largely true. However, for larger members cast in-place, the concrete cast from multiple trucks may have variable properties that will result in spatially variable material properties within a single concrete element. Wind turbine foundations, thick walls, tunnels, and deep mat foundations are examples of large structures that are typically designed without transverse shear reinforcement and with the assumption of homogenous materials; however, due to their size, they almost always consist of multiple batches of concrete. The comprehensive analysis of one such structure will provide new understanding of the potential implications of spatial variability on the performance of large shear-critical elements, such as failure mode, strength, ductility, and overall load-deformation response.

PLS4000 SPECIMEN

Specimen details

The specimen analyzed in this study was a large reinforced concrete slab strip denoted PLS4000. The slab strip was part of an investigation to assess the shear strength of very large unreinforced concrete slabs. For additional details pertaining to the construction, testing and results for PLS4000, refer to Collins et al.[6] and Quach.[7]

Figure 1 shows details of the slab strip that was tested under an off-center displacement-controlled point load, P, which divided the specimen into two shear spans labeled east and west. The west span was 7 m (23 ft) in length and contained vertical 20M T-headed reinforcing bars spaced at 1.5 m (4.9 ft). The east span was 12 m (39.4 ft) in length and had no shear reinforcement. The longitudinal reinforcement consisted of nine 30M reinforcing bars of Grade 500W, which equates to a reinforcement ratio of 0.656%. Three 20M bars were used for crack-control at the top of the slab strip. The specified thickness of the slab strip was 250 mm (10 in.).

ACI Structural Journal, V. 118, No. 2, March 2021.

MS No. S-2020-143, doi: 10.14359/51728194, received April 12, 2020, and reviewed under Institute publication policies.

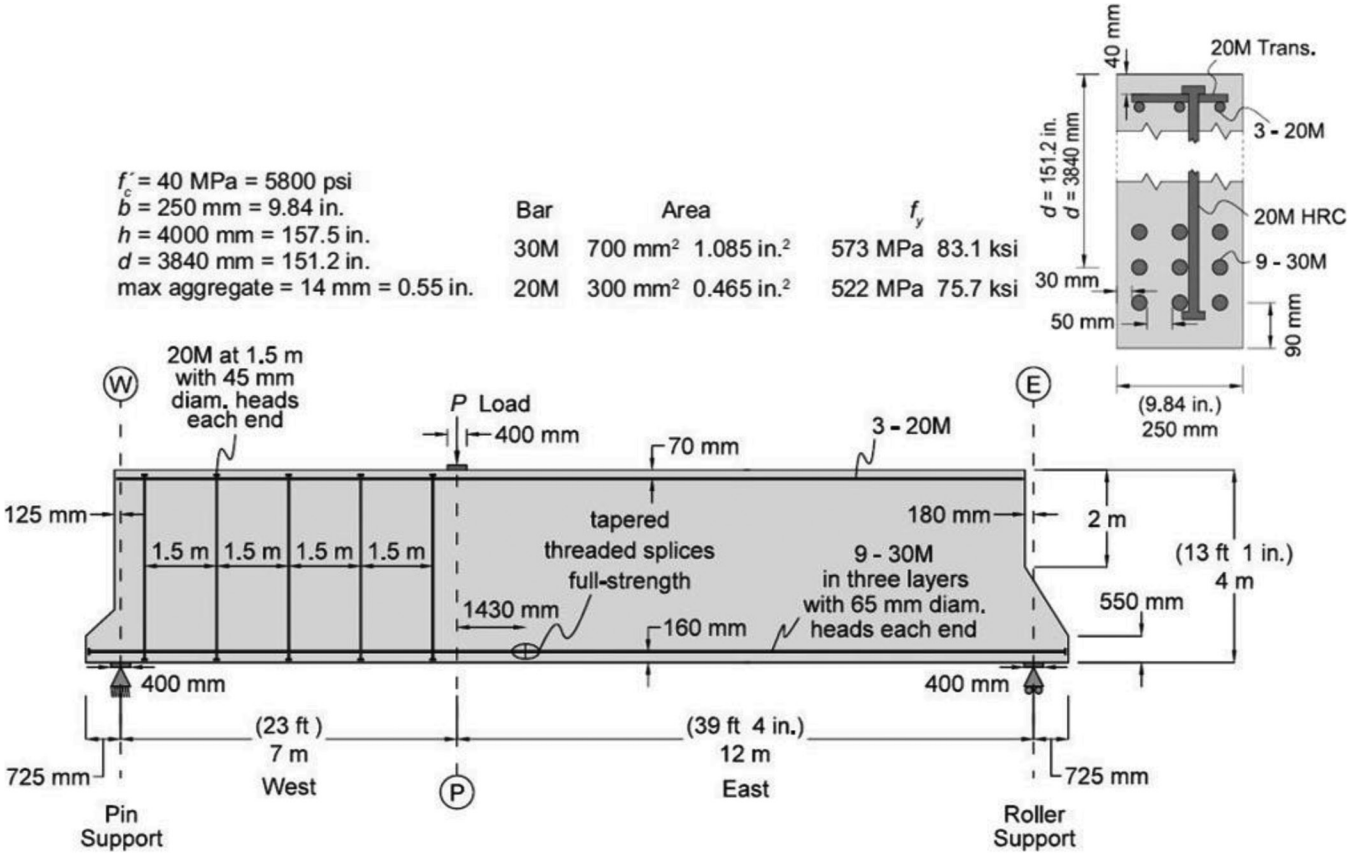

Fig. 1—Details of PLS4000 specimen (taken from Collins et al.[6]).

Two tests were performed to determine the capacities of the east and west spans. The slab strip was designed such that the first loading test would fail the east span, containing no transverse reinforcement. The east span was repaired using external post-tensioned vertical thread-bars; the specimen was loaded again, resulting in failure of the west end. For the purpose of this study, focus is placed on the behavior of the east span only.

Test results

The measured load-deformation response of the specimen is shown in Fig. 2 along with the crack diagram at failure. The significant self-weight of the specimen, measuring 442 kN (99.4 kip), produced a deflection of approximately 1.0 mm (0.04 in.). Flexural cracking occurred when the applied load (P) reached 198 kN (45 kip). Failure of the specimen was initiated by the development of a flexural-shear crack that propagated near the support, traversing the depth of the member at an inclination of approximately 45 degrees toward the loading point. At failure, the applied load was equal to 685 kN (154 kip) and the deflection at the point-load location was 12 mm (0.47 in.).

A prediction competition was organized on the behavior of PLS4000 specimen with 66 entries from around the world. Shown in Appendix A* is a comparison of the experimental results with the predictions in terms of the applied load to cause failure of the east span. Also shown on the plot are the calculated strengths based on six different code provisions. The predictions are marked by significant scatter, with 44% of the submissions dangerously unconservative and only 20% of the predictions considered sufficiently accurate. Collins et al.[6] concluded: *"predicting the shear strength of very thick slabs not containing shear reinforcement was a challenging task for the profession."*

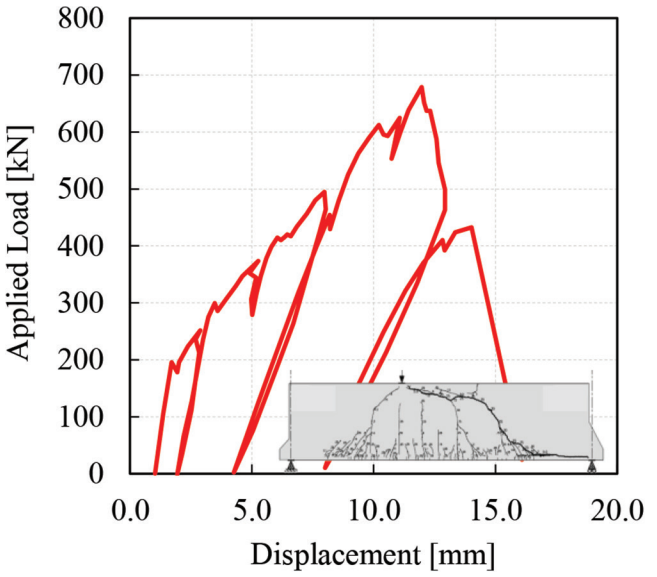

Fig. 2—Measured load-deformation response (adapted from Quach[7]).

*The Appendix is available at **www.concrete.org/publications** in PDF format, appended to the online version of the published paper. It is also available in hard copy from ACI headquarters for a fee equal to the cost of reproduction plus handling at the time of the request.

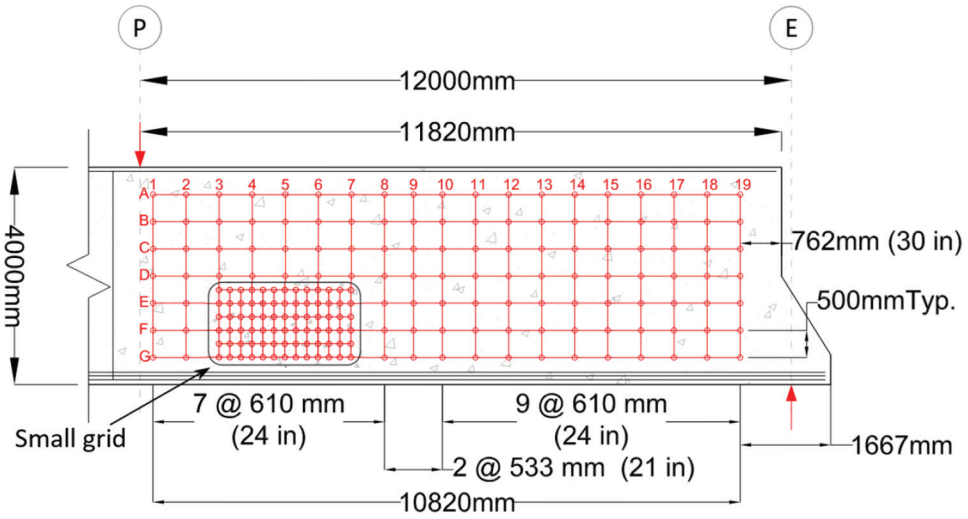

Fig. 3—Grid layout of ultrasonic pulse velocity testing.

TEST PROGRAM

Procedure

The objective of the collateral study was to determine if statistically significant spatial variability existed within the concrete, given the largeness of the specimen, by spatially mapping the compressive strength using nondestructive testing. The experimental program involved the collection of ultrasonic pulse velocity (UPV) measurements from the slab strip and from five sets of cylinders. Each set of cylinders contained two cylinders from each batch of concrete (three trucks were used in casting) for a total of six cylinders per set, 30 cylinders in total. The cylinders were tested at 7, 14, 22, 28, and 42 days after the cast.

For the UPV tests on the main slab strip, a set of grid points was established. Measurements were taken at increments of 500 mm (20 in.) in the vertical direction and between 610 and 533 mm (24 and 21 in.) in the horizontal direction. The variable spacing of the horizontal coordinates was selected such that the measurements would fall directly between surface seams caused by the formwork. The forms were constructed using prefabricated panels with either a width of 610 or 457 mm (24 or 18 in). At the joints between the panels, vertical and horizontal surface seams were created. Thus, to avoid the surface seams, the vertical gridlines were centered between adjacent defects. The grid layout is shown in Fig. 3. The grid was measured using a ruler that was suspended from the top of the slab strip. The ruler was leveled vertically, and each grid point was centered between seams. Horizontal and vertical grid points were then checked with a level and a tape measure.

In addition to the large grid, a smaller grid was established to capture a small section of the slab strip at a higher resolution, as illustrated in Fig. 3. The smaller grid added two vertical gridlines between each major vertical gridline, and one horizontal gridline between each major horizontal gridline. This created a vertical gridline spacing of approximately 200 mm (7.87 in.) and a horizontal gridline spacing of approximately 250 mm (9.84 in.).

The UPV instrument measures the travel time of an ultrasonic pulse. In order to determine the velocity, the thickness of the slab strip had to be assessed accurately. The original formwork required a series of ties passing through the width of the slab strip in order to hold the forms together. This left a set of holes though the slab strip that were used to measure the width of the slab strip.

Data collected

This section summarizes the test data obtained from the concrete cylinder tests, the UPV measurements, and the measured slab strip widths. Two concrete cylinders from each of the three trucks were tested at 7, 14, 22, 28, 35, and 49 days. The 28-day compressive strength of the concrete cylinders had an average value of 39.4 MPa (5710 psi). Table 1 summarizes the compressive strength values for the concrete from each truck, as measured by Quach.[7]

As part of the test program undertaken for the assessment of spatial variability of concrete, UPV measurements were performed for each cylinder. Due to scheduling issues, the UPV measurements were not collected for the 35-day cylinders. In addition, the UPV measurements for the 49-day cylinders were taken at 42 days. The UPV measurements are summarized in Table 1. A scatter plot of the measured UPV and compressive strength is presented in Fig. 4 which shows that a correlation exists between the UPV and the compressive strength of the concrete.

From the PLS4000 specimen, UPV measurements were taken on the main grid at a concrete age of 14 days and on the small grid at a concrete age of 15 days. At each grid point, five UPV measurements were recorded and averaged. To aid in the visualization of the data, a cubic spline interpolation of the main grid is shown in Fig. 5. From the figure, it is observed that there was distinct stratification in the vertical direction. The concrete was cast using three trucks, each with a lift height of approximately 1.0 to 1.5 m (3 to 5 ft). The UPV measurements were therefore consistent with concrete placement. Additionally, the cylinders from the second truck, when measured at 14 days, were consistently stronger than those from the other two trucks. This was reflected in the shorter travel time for the ultrasound wave that was observed. The travel time measurements ranged from 50.9 and 54.5 microseconds.

The small grid visualization is shown in Fig. 6. The smaller gird also reflected the stratification observed in the

Table 1—Compressive strength and UPV values for concrete cylinders

Age (days)		Compressive strengths (MPa)				Ultrasonic pulse velocity (m/second)				Length (mm)
		Truck 1	Truck 2	Truck 3	Average	Truck 1	Truck 2	Truck 3	Average	T1/T2/T3
7	A	27.0	31.8	31.6	30.0	4638	4735	4698	4662	301/298/294
	B	26.8	32.2	30.3		4609	4727	4566		296/299/297
14	A	32.7	34.9	37.3	35.7	4842	4844	4754	4814	299/295/299
	B	33.9	38.5	37.0		4793	4851	4801		296/293/299
22	A	37.3	36.9	38.0	37.2	4888	4860	4879	4873	304/296/304
	B	38.0	38.1	35.3		4900	4875	4834		303/297/304
28	A	38.5	35.6	42.6	39.4	4928	4935	4968	4932	300/303/302
	B	42.0	42.2	35.4		4860	4992	4910		301/301/304
35	A	37.5	42.1	38.9	41.5	—	—	—	—	—
	B	39.1	44.5	46.7		—	—	—		—
49	A	42.8	44.7	45.6	43.4	4944	4981	5033	5022	301/303/301
	B	40.6	42.6	44.2		5018	5012	5022		303/301/305

Note: 42 days for the UPV measurements. 1 MPa = 145 psi; 1 m = 3 ft; 1 mm = 0.04 in.

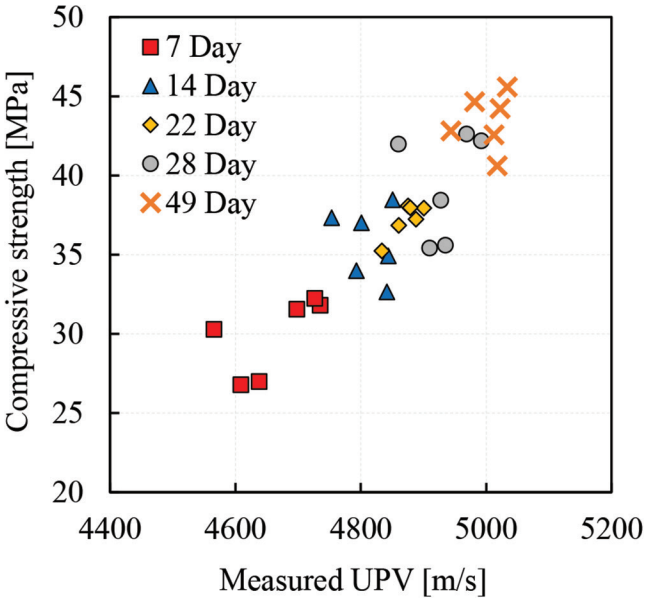

Fig. 4—Measured ultrasonic pulse velocity versus cylinder compressive strength.

main grid; however, it only straddled the bottom two lifts. The stratification boundary in both the main grid and the small grid appeared to be at an elevation of approximately 1.2 m (3.9 ft).

The thickness of the slab strip was measured through a series of holes that were present in the slab strip from the placement of the formwork ties. The slab strip thickness at each grid point was then determined by linear interpolation. The thickness was found to vary between 244 mm (9.6 in.) and 259 mm (10.2 in.), as discussed later. A contour of the measured thickness of the slab strip is shown in Fig. 7.

The ultrasonic pulse velocity was calculated using the measured times and the interpolated thickness. The UPV measurement is calculated using Eq. (1) where Δx is the measured thickness and Δt is the measured travel time. Figures 8 and 9 show the interpolated UPV measurements corrected for thickness variations.

$$UPV = \Delta x / \Delta t \tag{1}$$

Analysis of data

Thickness of PLS4000 specimen—The thickness of the slab strip showed little variation, ranging between 244 mm (9.6 in.) and 259 mm (10.2 in.). The variation of thickness was assumed to be a random variable. The distribution of thickness observed in the slab strip was found to be normally distributed with a mean value of 251 mm (9.9 in.) and a coefficient of variation of 1.0%. The fitted distributions are shown in Appendix B. Thickness spatial correlation is expected to exist as the thickness variation occurs due to changes in formwork. However, the experimental semivariogram, plotted in Appendix B, reveals that no such spatial correlation existed in the thickness (refer to Hunter[8] for more information on experimental semivariograms). This was due, in part to the difficulty of measuring the thickness through holes in the slab strip left from the formwork. As such, no statistically significant conclusion can be drawn about the spatial statistics of the slab strip thickness.

Concrete cylinder data—A regression model was used to relate the ultrasonic pulse velocities to the compressive strengths measured from cylinders, reported in Table 1. Additionally, temporal regression models were employed for the compressive strength and ultrasonic pulse velocity.

The regression model adapted from Unanwa and Mahan[3] was used to evaluate the change in concrete strength versus time. A linear relationship was assumed between the compressive strength, normalized from its 28-day strength, and the natural logarithm of the concrete age in days. Eq. (2) was developed accordingly to describe the compressive strength of concrete.

$$f_{c,t}' = (0.1632 \ln t + 0.4564) \cdot f_{c,28}' \tag{2}$$

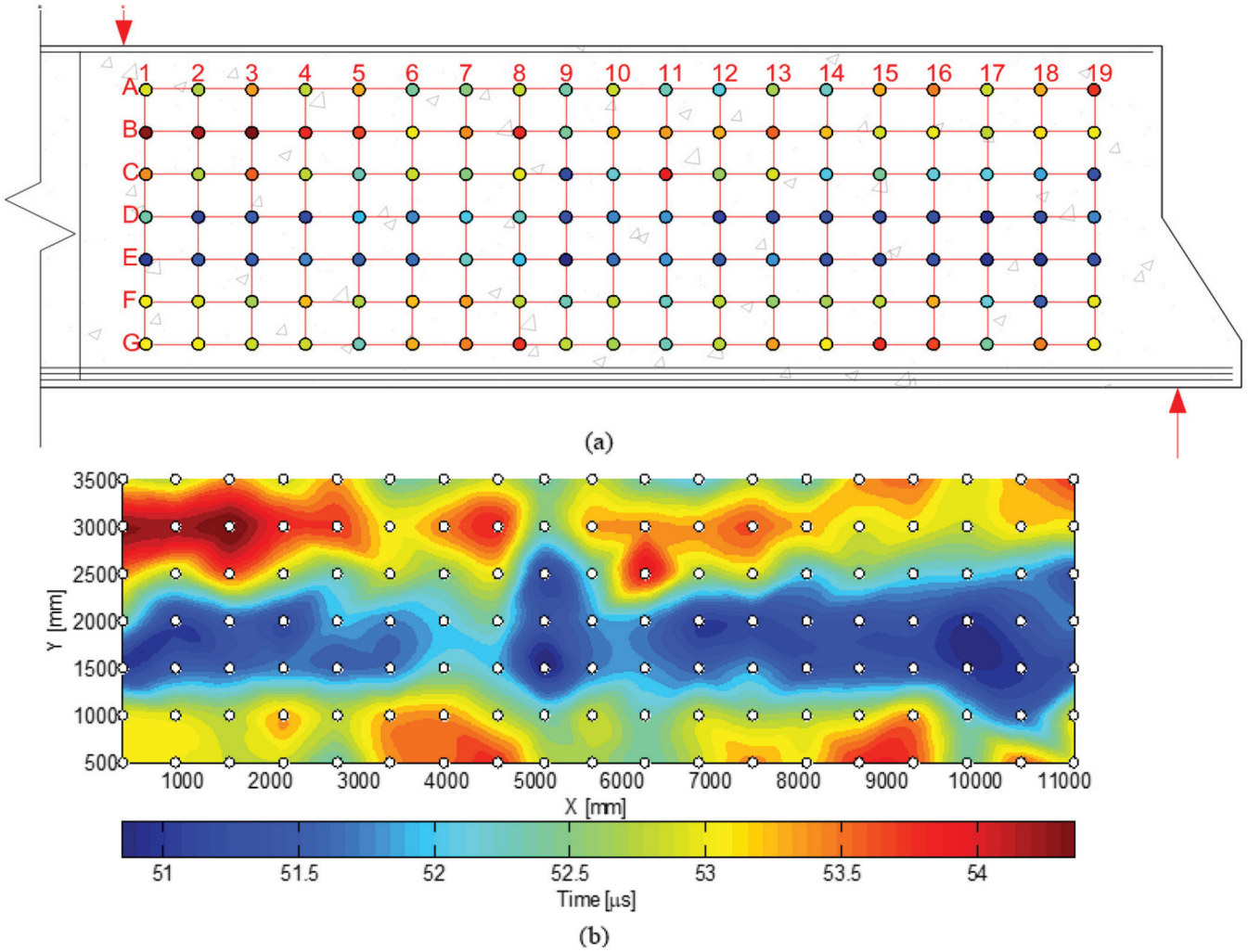

Fig. 5—UVP time measurements for main grid: (a) actual data; and (b) interpolated data.

The regression provided an R^2 value of 0.796 with respect to all cylinder compression tests. This was considered acceptable as the concrete contained both within-batch variation and batch-to-batch variation. A scatter plot of the collected data and the fitted regression is shown in Fig. 10(a). The regression is also compared against the average of the concrete strength at each test date in Fig. 10(a). The R^2 value of 0.986 with respect to the average compression strengths revealed good agreement between the test data and the selected regression model.

Equation (3) was developed to relate the evolution of ultrasonic pulse velocity with time. The regression produced a R^2 of 0.994 with respect to the average UPV measurements. The UPV measurements and the average of the UPV measurements are compared against the fitted trend in Fig. 10(b).

$$UVP_t = (0.038 \ln t + 0.8728) UVP_{28} \tag{3}$$

A third regression model was used to relate the ultrasonic pulse velocity to the compressive strength of concrete. Panesar and Chidiac[9] suggested that a linear relationship exists between the fourth root of the concrete strength and the ultrasonic pulse velocity. This relationship was assumed for the regression of the test data. Eq. (4) is the resulting regression equation. A plot of the fitted regression model with the average UVP and average compressive strengths is shown in Fig. 11. This plot reveals that the average values are in good agreement with the prediction model.

$$\left(f_c'\right)^{0.25} = \frac{UPV}{1640} - 0.4968 \text{ (MPa)} \tag{4}$$

The residuals from the regression model were analyzed as a random variable. The residuals have a mean of 0.051 MPa (7.39 psi) and a standard deviation of 2.24 MPa (325 psi). Least squares regression assumes of a normally distributed error term. A comparison of the empirical cumulative distribution function for the residuals and a fitted normal distribution confirms this assumption. A Kolmogorov–Smirnov (KS) test on the residuals confirmed the goodness of fit. Thus, a normal distribution is considered a good fit for the error parameter in the regression model. Plots of the residuals, empirical and assumed cumulative distribution functions are given in Appendix C.

Spatial analysis of UPV measurements—For the PLS4000 slab strip, the UPV measurements were all collected from the same concrete specimen. Thus, it was assumed that the UPV measurements were statistical data from the same population. The UPV was found to be normally distributed with a mean of 4793 m/s (15,700 ft/s) and a standard

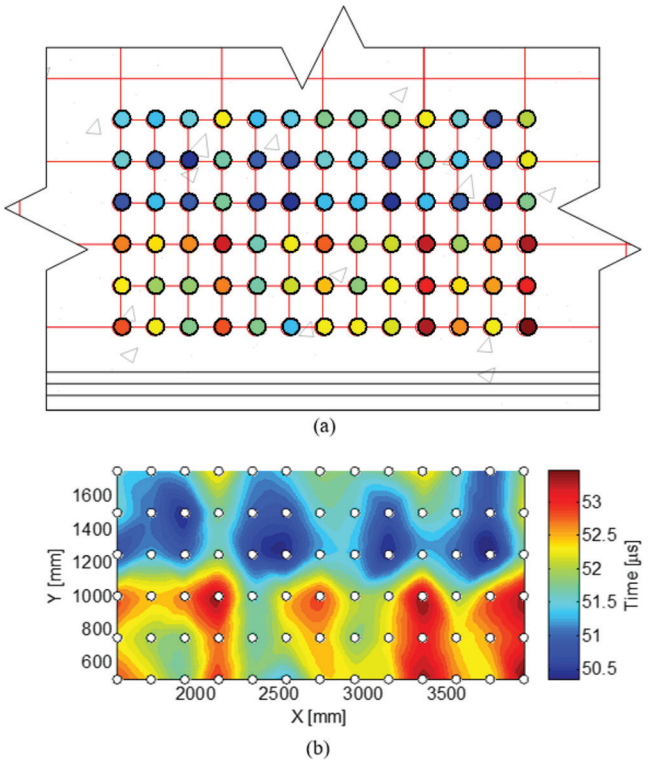

Fig. 6—UVP time measurements for small grid: (a) actual data; and (b) interpolated data.

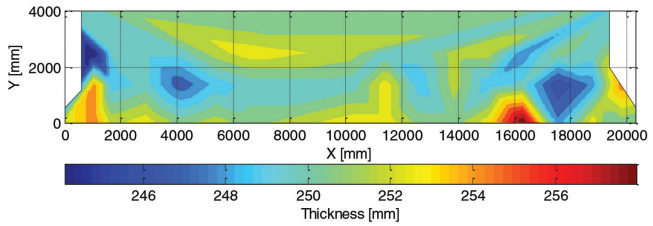

Fig. 7—Interpolated plot of measured thickness.

deviation of 82.9 m/s (272 ft/s). A KS test and a chi-squared goodness of fit test provided p-values of 0.211 and 0.505, respectively. The histogram and empirical cumulative distribution functions, as well as the fitted distribution, are shown in Appendix D.

The spatial variability of the UPV measurements was first assessed using ANOVA testing to determine if the variability between points is greater than the variability at a given point due to measurement error. This was done with a replicated two-way ANOVA test where the independent variables were the horizontal and vertical grid positions, and the dependent replicated variable was the measured UPV. The null hypothesis assumed that the concrete had uniform material properties everywhere regardless of concrete batch or location. The results of the ANOVA test are shown in Table 2.

The ANOVA test revealed that there was statistically significant variability between grid points. Both the X and Y directions had small p-values, suggesting that there was significant variability. In addition, there was no interaction between the X and Y variables. This implied that the variations in the X and Y directions were independent.

The data collected were assumed to be part of a random field. In order to interpolate between the sampled points, spatial statistical tools are required. An approach like Nguyen et al.[10] was adopted. An empirical semivariogram was constructed from the data set.

A semivariogram determines how the data are correlated with distance. As such, to predict random fields from collected spatial data, a semivariogram is required.[11] An empirical construction of the semivariogram is achieved by employing Eq. (5)

$$\hat{\gamma}(\mathrm{x}) = \frac{1}{2n(x)} \sum_{x_i - x_j = x} \{Z(x_i) - Z(x_j)\}^2 \tag{5}$$

where the lag distance, x, is defined as the distance between two points x_i and x_j, $\hat{\gamma}(x)$ is the empirical semivariance for a lag distance x, $n(x)$ is the number of pairs of the lag distance x within the data set, and $Z(x_i)$ and $Z(x_j)$ are the measured values of the random field Z for points x_i and x_j respectively. The random field Z was defined as the variation of ultrasonic pulse velocity within the concrete slab strip. Note that the assumed random field is two-dimensional. Thus, the value $x = x_i - x_j$ is generalized in two dimensions to be the actual distance between two points and is calculated as $x = \sqrt{\Delta X^2 + \Delta Y^2}$. Stein[11] noted that sets of x are not entirely equal in value. Therefore, they are usually grouped into bins of similar lag distances.

The random field was assumed to have an autocorrelation function. An autocorrelation function is a function that describes the covariance of a random field by the distance between two points within the field.[11] This is formally described by Eq. (6)

$$\mathrm{cov}\{Z(x), Z(y)\} = K(x - y) \tag{6}$$

where $\mathrm{cov}\{Z(x), Z(y)\}$ is the covariance between any two points x and y in the random field Z. $K(x\text{-}y)$ is the autocorrelation function that can describe the covariance for any two points x and y based on their difference. Again, note that if the random field is higher than one-dimensional, then the quantity $x\text{-}y$ is the vector length between vectors x and y. The commonly used isotropic autocorrelation function is the spherical model shown in Eq. (7)

$$K(r) = \begin{cases} C\left[1 - \dfrac{3r}{2a} + \dfrac{r^3}{2a^3}\right] & r \le a \\ 0 & r \rhd a \end{cases} \tag{7}$$

where the variance of the random field is described by $C + C_0$, the parameter C_0 is equal to the nugget effect, r is the lag distance equal to $x\text{-}y$, and a is the range of the random field. The nugget effect describes the phenomenon where points at a very close (or the same) distance still exhibit stochastic variability. This is also referred to as the micro-scale variation. The range of a random field is the distance at which two points are no longer correlated. The parameter C is the amount of variance in the random field that is not attributed

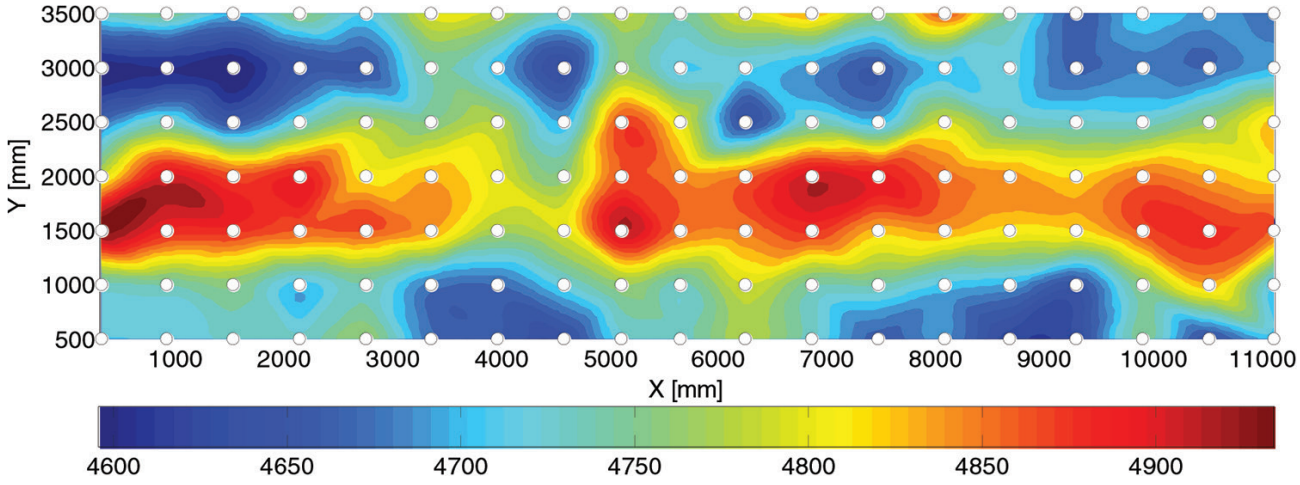

Fig. 8—Calculated UPV for large grid with cubic spline interpolation.

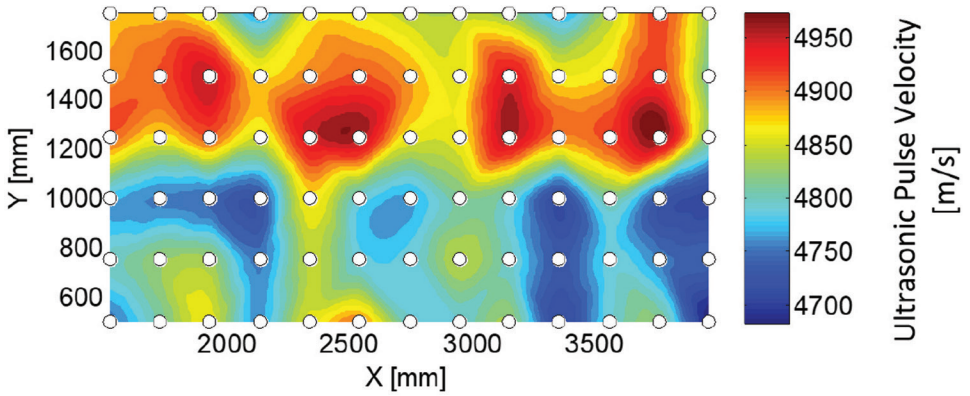

Fig. 9—Calculated UPV for small grid with cubic spline interpolation.

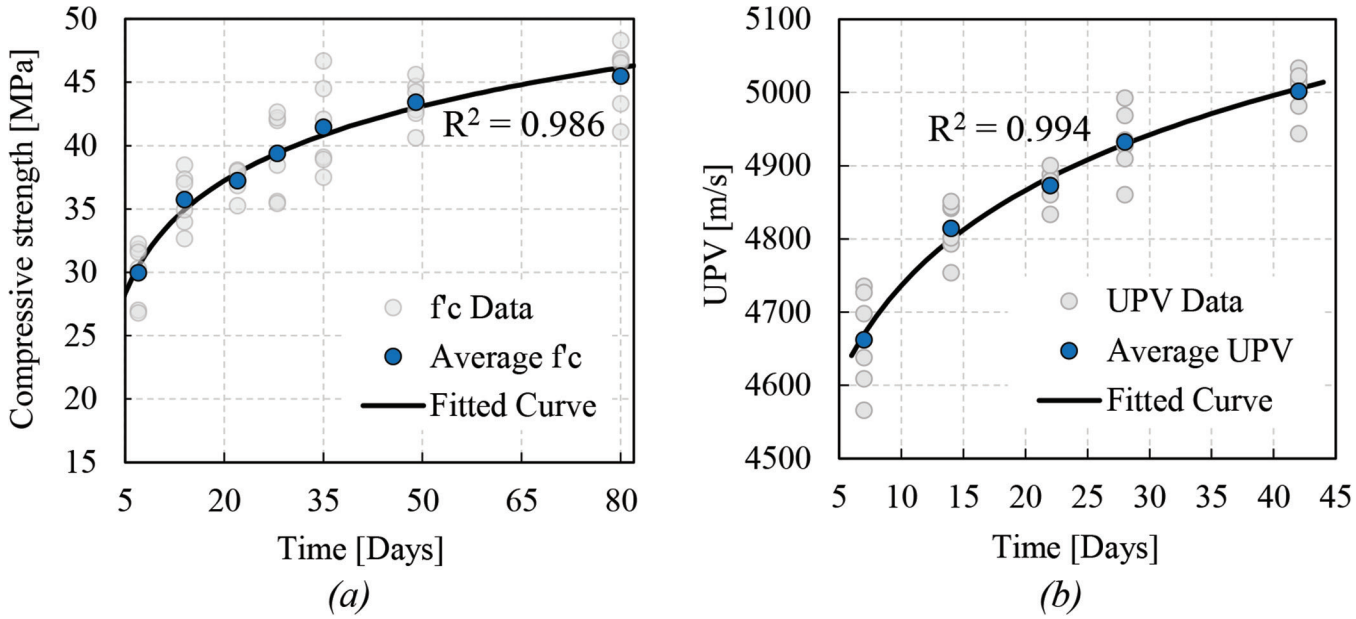

Fig. 10—(a) Average daily compressive strength compared against fitted regression; and (b) average ultrasonic pulse velocity compared against regression model.

to spatial variation. The analytical semivariagram can be determined from Eq. (8)

$$\gamma(r) = \text{var}\{Z\} - K(r) \tag{8}$$

Table 2—Replicated two-way ANOVA analysis results

Source of variation	Sum of squares	Degrees of freedom	Mean square	F test-ratio	p-value
X-direction	47.7	18	2.65	3.56	1.2×10^{-6}
Y-direction	42.5	6	7.04	9.48	6.6×10^{-10}
Interaction	14.6	108	0.13	0.18	1.00
Error	395.4	532	0.74	—	—
Total	499.9	664	—	—	—

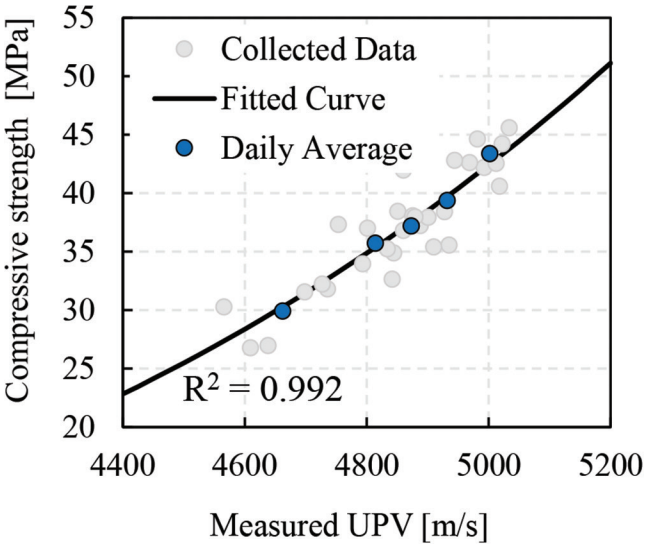

Fig. 11—Average UVP versus average compressive strength and regression model.

Substituting the variance of the random field with $C + C_0$ yields Eq. (9)

$$\gamma(r) = \begin{cases} C_0 + C\left[\dfrac{3r}{2a} - \dfrac{r^3}{2a^3}\right] & r \le a \\ C_0 + C & r \rhd a \end{cases} \tag{9}$$

The spherical model was assumed to represent the data. A regression was done to determine the range, sill, and nugget effect. The regression model is plotted with the empirical semivariogram in Appendix D. The semivariogram was found to have no nugget effect; the sill of the semivariogram was calculated to be 6810 m^2/s^2 (73,300 ft^2/s^2), and the range was calculated to be 1190 mm (48.9 in.).

Using the properties of an assumed semivariogram, an ordinary kriging map can be generated from the collected data points. Kriging maps are heavily employed in geospatial interpolation problems.[11] Shown in Appendix E is a summary on how the kriging maps are calculated. This method was used to produce kriging maps for the ultrasonic pulse velocity at the center of each of the finite elements in the mesh. The calculated kriging map for the ultrasonic pulse velocity is shown in Fig. 12.

Ultrasonic pulse velocity variable transformation—In order to convert the data from the kriging map of the ultrasonic pulse velocity to concrete compressive strengths at test day, Eq. (3) was used to transform the data in two stages. The UPV data were transformed from the measured 14-day values to the 28-day values. Then, these UPV values were transformed from the predicted 28-day values to the test day (46-day) values. The calculated transformation factor was equal to 1.047 and was used as a multiplier to transform the UPV data measured at 14-day to 46-day values.

Then, Eq. (4) was used to calculate the corresponding compressive strength. To assess the accuracy of this transformation, Eq. (3) and Eq. (4), based on data from 7 to 49 days, were compared against Eq. (2), based on data up to 80 days

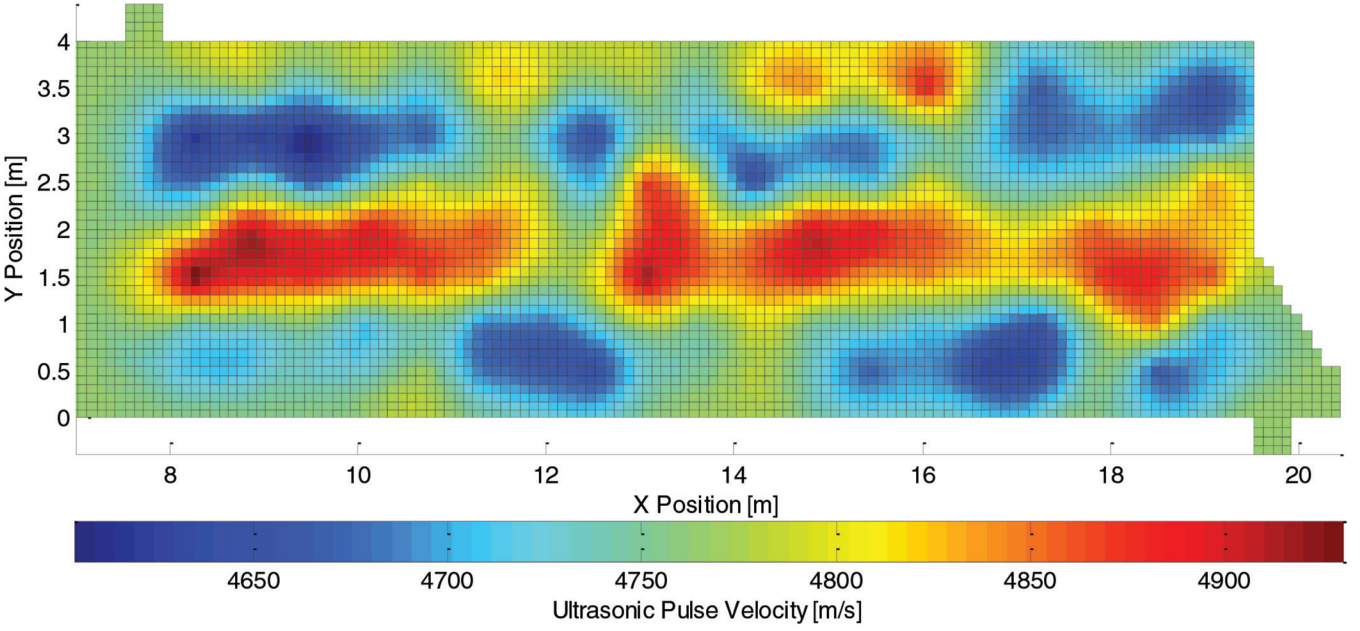

Fig. 12—Kriging map used for finite element analysis.

Table 3—Statistical parameters for concrete cylinder test data

Age (days)	Mean f_c'	σ (MPa)	COV (%)
7	29.96	2.45	8.18
14	35.74	2.23	6.24
22	37.23	1.08	2.91
28	39.39	3.35	8.51
35	41.46	3.59	8.66
49	43.42	1.79	4.11
80	45.47	2.71	5.95
Mean COV			6.37

Note: σ is Standard deviation; COV is coefficient of variation; 1 MPa = 145 psi.

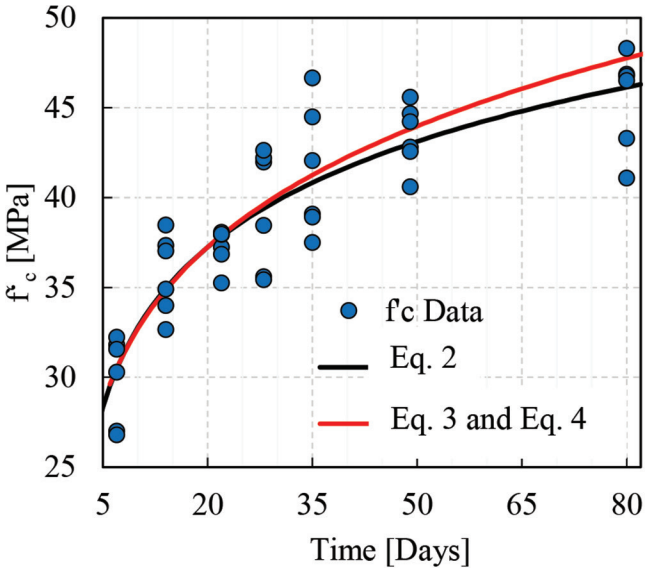

Fig. 13—Comparison of fitted and calculated compressive strength trend.

in Fig. 13. The error in the collected data for interpolating between 0 and 49 days was reasonably low. However, the trend started to deviate from the Eq. (2) when extrapolating past 49 days. Testing of PLS4000 ended on day 46, thus, the interpolation was considered reasonably accurate. Figure 14 shows the finite element model inputs after the kriging map and variable transformation were applied. The compressive strength for each element was an input variable. The tensile strength was calculated based on the ACI 318[12] relationship recommended for web-shear cracking as per Eq. (10). The modulus of elasticity, E_c, was calculated using the equations recommended in the CSA A23.3[13] code (Eq. (11))

$$f'_{t.ACI} = 0.33\sqrt{f'_c}(\text{MPa}) \tag{10}$$

$$E_c = \left(3300\sqrt{f'_c} + 6900\right)\left(\frac{\gamma_c}{2300}\right)^{1.5}(\text{MPa}) \tag{11}$$

where γ_c is density of concrete, taken as 2300 kg/m^3 (143.6 lb/ft^3).

Within member strength variation and spatial variability—To assess the spatial variability, the variability attributed to batch-to-batch variation must be disaggregated from the variability of the test. It has been shown in the literature that the within-member variation is inflated when the number of batches of concrete cast within a member increases.[14]

The variability due to multiple batches cast in the same member was assessed using the cylinder data. The statistics for each of the cylinders is presented in Table 3.

The total coefficient of variation of the UPV test data after regression, V_{EXP}, was calculated to be 0.0784. This coefficient of variation includes the variability due to spatial variation, and due to batch-to-batch variation. Using the mean coefficient of variation from Table 3 as the batch-to-batch coefficient of variation ($V_{Batch\text{-}to\text{-}Batch}$), the coefficient of variation due to spatial variability (V_S) can be calculated using Eq. (12).

$$V_S = \sqrt{V_{EXP}^2 - V_{Batch-to-Batch}^2} = 0.0457 \tag{12}$$

Bartlett and MacGregor[14] analyzed the spatial variation within a set of girders originally tested by Scanlon and Mikhailovsky.[15] They reported that the average coefficient of variation for variation due to within-girder spatial variation was 0.043. Thus, the coefficient of variation due to spatial variability in this study was considered reasonable. It should be noted, however, that the influence of variability due to UPV measurement error was not included and should be addressed in a future study.

Comparison of spatial variability and experimental crack pattern

Figure 15 shows an overlay of the experimental crack pattern and the collected UPV data. Cracking in reinforced concrete is influenced by the stress field and the local strength variations. A study conducted by Koide et al.[16] showed that probabilistic cracking in unreinforced sections deviated from a deterministic uniform approach. Thus, it is possible that in a large unreinforced section, where the failure depends on the transfer of stress along the crack, that the material properties play a role in the crack pattern. In Fig. 15, it can be observed that that the two main shear cracks pass between the zones of weakness in the middle layer. This suggests that the variation in tensile strength in the middle layer contributed to the location of cracks and ultimately to the location of the failure crack.

FINITE ELEMENT ANALYSIS OF PLS4000

The nonlinear finite element analysis program VecTor2[17,18] was used for the analysis of PLS4000 specimen. This program is based on a smeared-crack macro-modeling approach and is suited for the analysis of two-dimensional reinforced concrete structures. The theoretical basis of the program is the Modified Compression Field Theory[19] and the Disturbed Stress Field Model.[20] Three type of analyses were performed. First, the slab strip was modeled with uniform mechanical properties. A subsequent analysis was performed to include the spatially variable properties

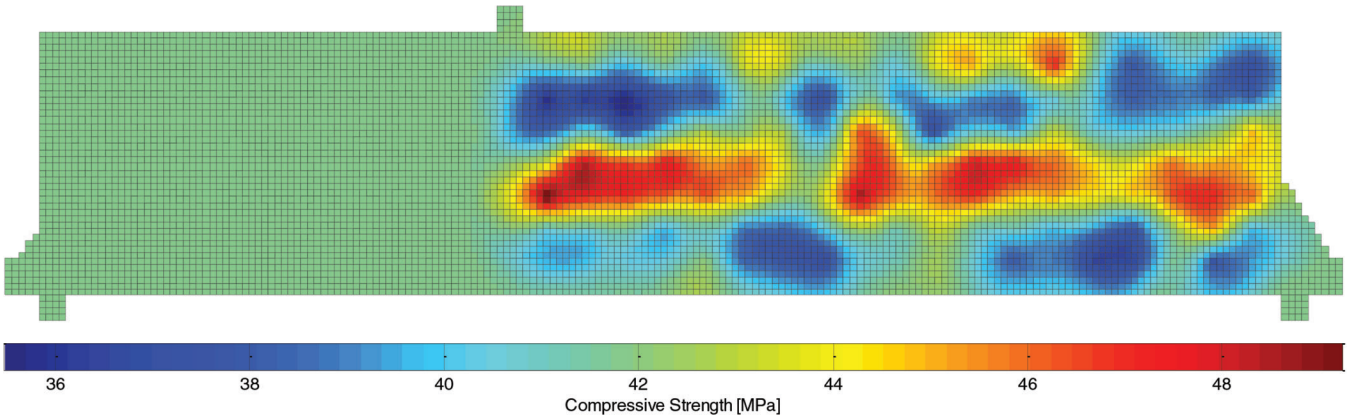

Fig. 14—Finite element model inputs with spatial variation of concrete material properties.

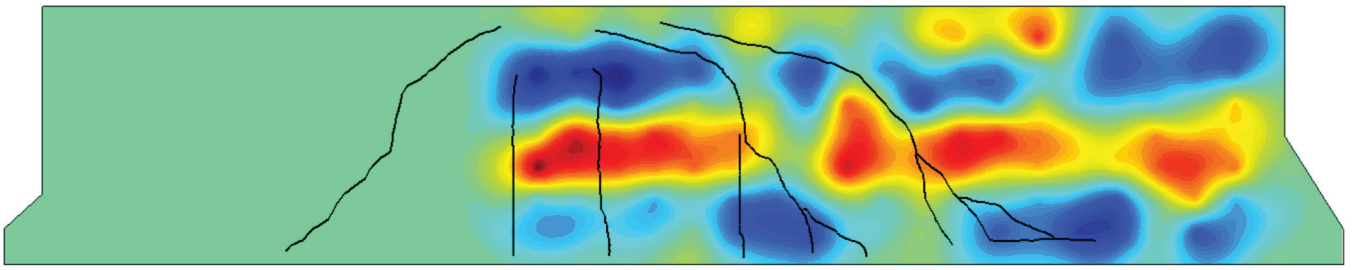

Fig. 15—Experimental crack pattern and Kriging map of collected UPV data.

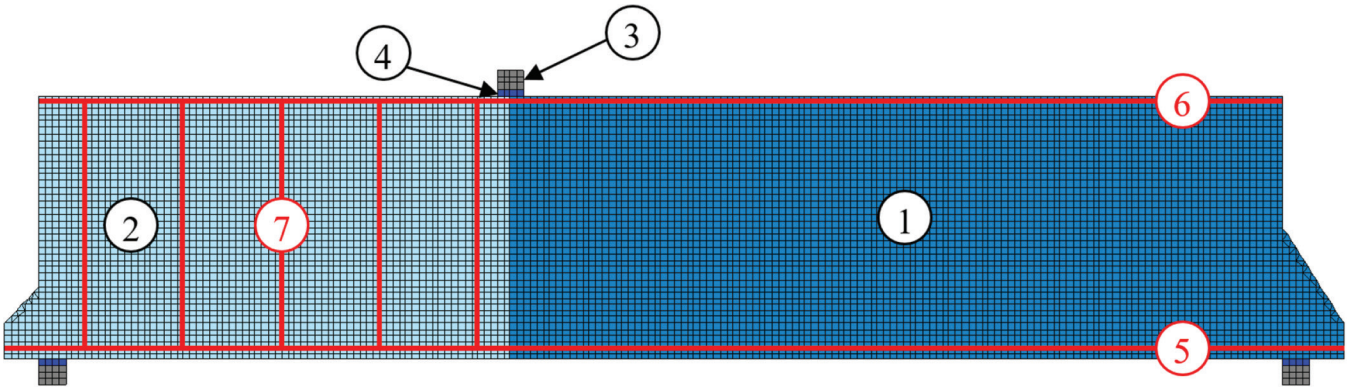

Fig. 16—Finite element mesh.

shown in Fig. 14. Lastly, a stochastic simulation was conducted to assess the sensitivity of the load-deformation response to different material input parameters.

Deterministic results

The finite element (FE) model constructed to model the PLS4000 specimen is shown in Fig. 16. A very fine mesh of 8033 elements was used to model the structure, with 41 elements used through the depth of the beam. The response is particularly sensitive to the assumed crack spacing and tension softening models. Therefore, the east and west spans of the beam were modeled using different material types due to the different assumed maximum crack spacing. CEB-FIP 1978 Code[21] equations were used to calculate the predicted crack spacing on either side; for the unreinforced side, the crack spacing was calculated to be 4035 mm (160 in.). The reinforcement was represented using discrete truss bar elements. The bottom and top flexural reinforcement were grouped into one set of truss bars with total areas acting through the geometric centroid of each bar group. A summary of the model inputs is shown in Table 4.

A comparison of the FE analysis and the experimental load-deflection response is shown in Fig. 17. The FE model predicted a failure load of 715 kN (161 kip) and a deflection at ultimate of 12.3 mm (0.484 in.). The analysis captured the initial and post-cracking stiffness of the structure; however, the cracking load predicted by the FE model was about twice that of the experiment, which could contribute to the offset observed in the post-cracking stiffness. This deterministic analysis with uniform material properties was submitted as an entry for the prediction competition organized by Collins et al.[6] before the physical testing began. The crack pattern, also shown in Fig. 17, was captured reasonably well.

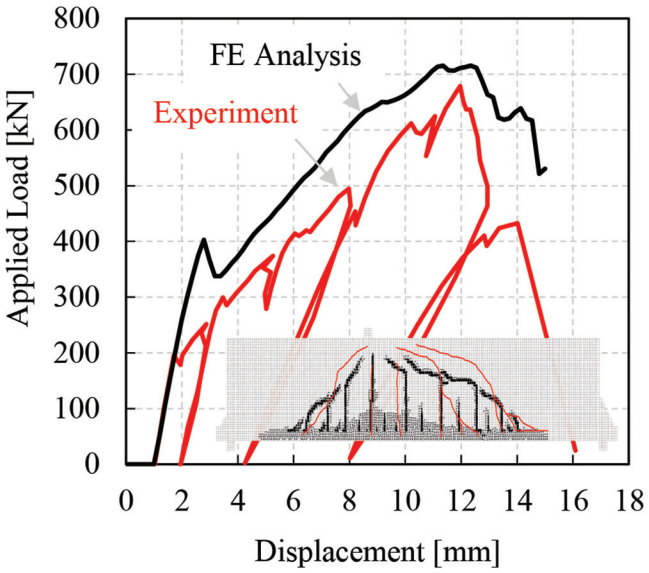

Fig. 17—Load-deflection for FE analysis with uniform properties versus experimental results.

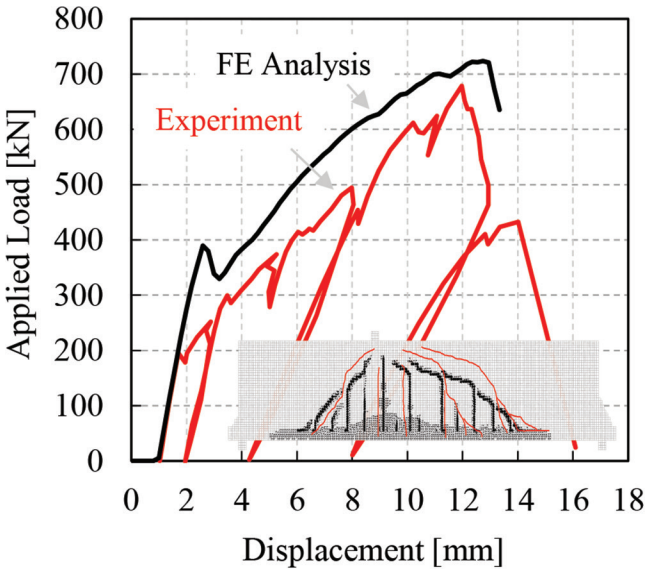

Fig. 18—Load-deflection for FE analysis with spatial variation versus experimental results.

Modeling spatial variability

The finite element model with uniform properties was updated to include the spatially variable properties shown in Fig. 14. An additional input file read in scaling factors that changed the compressive strength, tensile strength, and modulus of elasticity of the original model to match that of the measured test data. The FE model predicted a maximum load of 725 kN (163 kip) and a deflection at ultimate of 12.7 mm (0.5 in.). Figure 18 compares the analytical load-deflection response with the experimental results. Figure 18 also shows the experimental crack (red) pattern overlaid with the predicted crack pattern (black).

The resulting crack patterns and load-deflection responses obtained from the analysis including spatial variability and the analysis with uniform mechanical properties were almost identical, deviating only after the peak load. Most likely, the minimal difference between modeling techniques can be attributed to the underlying assumptions of the selected software. In the program used in this study, the compressive strength of an element is reduced when the crack width passes a given threshold. This is intended to simulate the loss in aggregate interlock when the crack widths become large. It the current formulation, the maximum crack width check is appropriate for capturing failure of concrete sections with no transverse reinforcement; however, it results in a model where the peak load is highly sensitive to the maximum crack spacing calculated in the analysis.

Stochastic analysis

Stochastic simulation was conducted on PLS4000 to assess the sensitivity of the load-deformation response to the material input parameters. A total of 175 simulations were conducted for the specimen.

Three stochastic input parameters were compared against four load-deformation response metrics. The selected metrics were the ultimate load, the deflection at ultimate loading, the initial uncracked stiffness, and the cracked stiffness. The ultimate load and corresponding displacement were determined by finding a local maximum that results in a change in tangent slope and a drop from the local peak load of greater than 10%. The uncracked and cracked stiffness coefficients were determined by linear regression. For

Table 4—Finite element model material properties

Color/material	ID	f_c'/f_y (MPa)	E_c/E_s (MPa)	$\varepsilon_c'/\varepsilon_u \times 10^{-3}$	f_t'/f_u (MPa)	t/A_s (mm/mm^2)	Description
Concrete	1	40	28,800	2.13	2.17	250	Concrete West span
Concrete	2	40	28,800	2.13	2.17	250	Concrete East span
Steel	3	500	200,000	5.00	600	250	Bearing plate steel
Bearing	4	N/A	28,800	N/A	N/A	250	Bearing material
Steel	5	573	20,000	14	685	6300	Bottom bars
Steel	6	522	20,000	17	629	900	Top bars
Steel	7	522	20,000	17	629	300	Vertical bars

Note: f_c' is compressive strength; f_y is yielding strength; E_c/E_s is concrete/steel modulus of elasticity; ε_c' is strain at peak stress; ε_u is ultimate strain; f_t' is concrete tensile strength; f_u is steel ultimate strength; t is thickness; and A_s is steel cross-sectional area; 1 MPa = 145 psi; and 1 mm = 0.04 in.

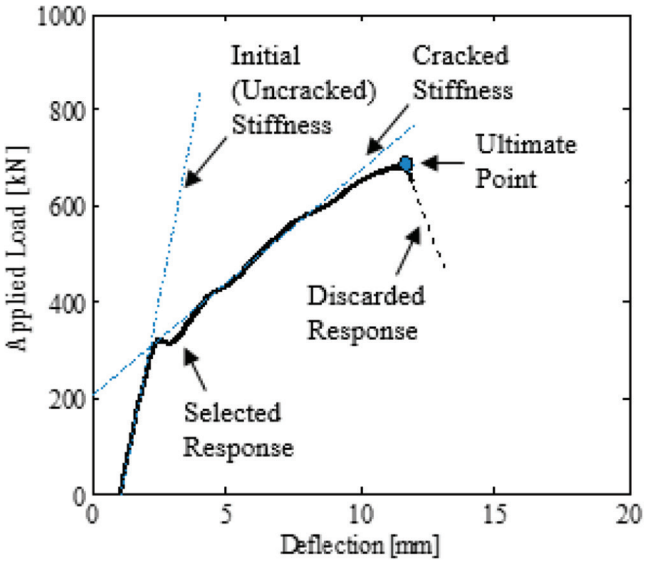

Fig. 19—Automated retrieval of simulation metrics.

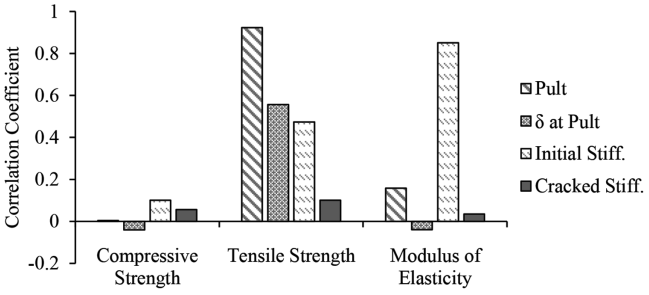

Fig. 20—Correlation coefficients for PLS4000 simulation results.

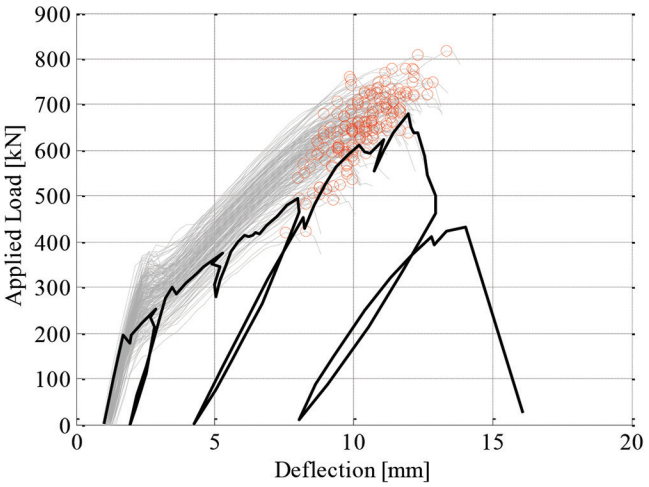

Fig. 21—Stochastic simulation results versus experimental load-deflection response.

the cracked portion of the load-deformation response, the cracked portion was isolated by removing all data with a deflection of less than 4 mm and all data above 75% of the ultimate deflection. An example of the automated retrieval of the four metric is shown in Fig. 19.

The three main stochastic parameters included in the simulations were the compressive strength, the tensile strength, and the modulus of elasticity. Each of these parameters was assumed to be an independent random variable for the simulation; however, the mean tensile strength and mean modulus of elasticity were calculated based on the compressive strength. Additional information on the stochastic analysis approach is summarized in Appendix F and presented in detail elsewhere.[22] The correlation coefficients for these three parameters with the four selected metrics were calculated. The correlation coefficients are a useful tool to determine which input parameters influence the load-deformation predictions. The correlation coefficients are shown in Fig. 20.

It can be seen from the results that the ultimate load and corresponding displacement are heavily influenced by the distribution of the tensile strength. The correlation coefficient for tensile strength and ultimate load is 0.92. This suggests that the tensile strength is the main contributor to the stochastic variation in member strength. The failure of an unreinforced section in VecTor2 is influenced by the maximum crack spacing and the tension softening response. The maximum crack spacing is constant for this analysis and thus, the tension response, which is directly related to the tensile strength, governs the variability. As previously mentioned, the compressive strength is generated independently of the tensile strength. The correlation coefficient between the compressive strength and the tensile strength is –0.052 which confirms the independence of the sampling. It is generally accepted that a correlation between the tensile strength and the compressive strength exists, and the correlation coefficient for the compressive strength typically should not be as low as shown in Fig. 20.

The initial stiffness is highly correlated with the modulus of elasticity. This is expected as the behavior is essentially linear elastic until significant cracking occurs. The tensile strength is also correlated with the initial stiffness, with a correlation coefficient of 0.47. Analytically, when cracking develops, the structure will retain stiffness until larger, wider cracks form. These larger cracks are what result in the cracked stiffness observed in the load-deformation response. However, the smeared cracks influence the initial stiffness of the load-deformation response and thus, a correlation is observed. The post-cracking stiffness appears to be independent of the input parameters. It likely is a function of the location of the wide cracks and the longitudinal reinforcement, which is only partially influenced by the spatially variable input parameters.

A plot of the experimental results with the stochastic simulation is shown in Fig. 21. This chart illustrates a few trends in the simulation. The initial stiffness and cracked stiffness of the experimental results are well captured by the stochastic simulations. The average concrete cylinder strength at the test date was 43.4 MPa (6295 psi). The simulation mean compressive strength was 38.5 MPa (5584 psi). Thus, the mean simulated peak load of 652 kN (147 kip) was considered to be reasonably close to the experimental peak load of 685 kN (154 kip).

The peak load and peak deflection were both found to be normally distributed random variables. Confidence intervals at a 99% confidence level for peak load and associated deflection were calculated as:

$$509 \text{ kN } (114 \text{ kip}) \leq P_{Ult.} \leq 795 \text{ kN } (178 \text{ kip}) \quad (13)$$

$$8.15 \text{ mm } (0.321 \text{ in.}) \leq \delta_{@P_{Ult.}} \leq 12.43 \text{ mm } (0.489 \text{ in.}) \quad (14)$$

The stochastic simulation reveals the large variability in strength and load-deflection response that may be present in this structure, were it built in the field. When performing stochastic simulations with the program, the full interaction between stochastic inputs and simulation outputs can be analyzed. Multiple failure modes can be identified and disaggregated, and lower bound estimates for deflection or resistance can be established. These estimates are useful for designing capacity protected elements or structural elements with stringent deflection tolerances. Additionally, the results of a stochastic simulation can be used in a reliability analysis.

CONCLUSIONS

Cracking in reinforced concrete is inherently stochastic. The cracks form at a lowest energy state as a combination of applied tensile stress and material weakness. This study measured the spatial variation present within a large shear-critical concrete specimen containing no shear reinforcement. The study succeeded in identifying statistical properties of the reinforced concrete. The collected UPV data provided evidence that the strength and failure mode of the unreinforced span is partially affected by the material variability. Both large shear cracks occurred between local planes of weakness observed within the middle layer of the concrete. This suggests that the propagation of shear cracks is influenced by zones of weakness in the concrete, and not just by the prevailing stress conditions.

UPV measurements have been identified as an adequate means of measuring material properties within the specimen and could be used to provide insight into how spatial variation affects a population of structures.

A model with uniform material properties may not capture the exact crack pattern, however a reasonable estimate of the load-deflection can be obtained with careful selection of model parameters. In the analyses conducted herein, the inclusion of spatial variation did not affect the failure mode significantly for the one specimen examined.

Future work on this topic should investigate the influence of spatial variation on the response of structures subjected to symmetric loading. In a symmetrically loaded shear-critical concrete member, spatial variation may have a significant effect on the location and propagation of the failure crack. In a uniform analysis, a large shear crack will form on both sides of the structure simultaneously. This deviates from experimental results, in which typically a single crack will form on one side of the specimen.

For the variations in concrete properties that can be expected in large field structures, there is a substantial influence on cracking pattern, stiffness, ultimate strength, and potentially even in the failure mode. This should be recognized when assigning confidence to the design strength of large shear-critical structures.

AUTHOR BIOS

Mark D. Hunter *is an Associate Principal at Quinn Dressel Associates in Toronto, ON, Canada. He received his BASc from the University of Waterloo, Waterloo, ON, Canada, and his MASc from University of Toronto, Toronto, ON, Canada. His research interests include stochastic finite element analysis of reinforced concrete structures.*

Anca C. Ferche *received her PhD from the University of Toronto in 2020. Her research interests include performance assessment and analysis of concrete structures, structural implications of deterioration mechanisms, and sustainability of concrete structures.*

Frank J. Vecchio, *FACI, is a Professor in the Department of Civil and Mineral Engineering at the University of Toronto. He received the following ACI awards: Structural Research Award (1998), Structural Engineering Award (1999), Wason Medal (2011), Joe Kelley Award (2016), and Arthur J. Boase Award (2020). His research interests include advanced constitutive modeling and analysis of reinforced concrete, assessment and rehabilitation of structures, and response to extreme loads.*

ACKNOWLEDGMENTS

The authors would like to acknowledge IC-IMPACTS and NSERC for funding support provided to this project. The authors would also like to acknowledge P. Quach, E. Bentz, and M. Collins for their generous sharing of information related to PLS4000, which was being done concurrent with this work. Lastly, the authors wish to acknowledge D. Panesar for sharing her UPV testing equipment. Without the generous contributions of the above, the present work could not have been completed.

REFERENCES

1. Mirza, S. A.; Hatzinikolas, M.; and MacGregor, J. G., "Statistical Descriptions of Strength Of Concrete," *Journal of the Structural Division*, V. 105, No. 6, 1979, pp. 1021-1037. doi: 10.1061/JSDEAG.0005161

2. Bartlett, F. M., and MacGregor, J. G., "Statistical Analysis of the Compressive Strength of Concrete in Structures," *ACI Materials Journal*, V. 93, No. 2, Mar.-Apr. 1996, p. 158-168

3. Unanwa, C., and Mahan, M., "Statistical Analysis of Concrete Compressive Strengths for California Highway Bridges," *Journal of Performance of Constructed Facilities*, ASCE, V. 28, No. 1, 2014, pp. 157-167. doi: 10.1061/(ASCE)CF.1943-5509.0000404

4. Stewart, M. G., "Spatial Variability of Pitting Corrosion and Its Influence on Structural Fragility and Reliability of RC Beams in Flexure," *Structural Safety*, V. 26, No. 4, 2004, pp. 453-470. doi: 10.1016/j.strusafe.2004.03.002

5. Li, Y., "Service Life Prediction And Repair of Concrete Structures with Spatial Variability," *HERON*, V. 52, No. 4, 2007, pp. 251-268.

6. Collins, M. P.; Bentz, E. C.; Quach, P. T.; and Proestos, G. T., "The Challenge of Predicting the Shear Strength of Very Thick Slabs," *Concrete International*, V. 37, No. 11, Nov. 2015, pp. 29-37.

7. Quach, P., "Understanding and Safely Predicting the Shear Response of Large-Scale Reinforced Concrete Structures," master's thesis, 2016, University of Toronto.

8. Hunter, M. D., "Towards Stochastic Finite Element Analysis of Reinforced Concrete Structures," MASc. Thesis, 2016, University of Toronto, Toronto, ON, Canada.

9. Panesar, D. K., and Chidiac, S. E., "Ultrasonic Pulse Velocity for Determining the Early Age Properties of Dry-Cast Concrete Containing Ground Granulated Blast-Furnace Slag," *Canadian Journal of Civil Engineering*, V. 34, No. 5, 2007, pp. 682-685. doi: 10.1139/l07-039

10. Nguyen, N. T.; Sbartaï, Z.; Lataste, J.; Breysse, D.; and Bos, F., "Assessing the Spatial Variability of Concrete Structures Using NDT Techniques – Laboratory Tests and Case Study," *Construction and Building Materials*, V. 49, 2013, pp. 240-250. doi: 10.1016/j.conbuildmat.2013.08.011

11. Stein, M. L., *Interpolation of Spatial Data: Some Theory for Kriging*, 1999, New York, Springer.

12. ACI Committee 318, "Building Code Requirements for Structural Concrete (ACI 318-14) and Commentary (ACI 318R-14)," American Concrete Institute, Farmington Hills, MI, 2019, 520 pp.

13. CSA A23.3-14, "Design of Concrete Structures," CSA Group, Mississauga, ON, Canada, 2014, 456 pp.

14. Bartlett, F. M., and MacGregor, J. G., "Assessment of Concrete Strength in Existing Structures," *Structural Engineering Report No. 198*, 1994, University of Alberta, Edmonton, AB, Canada.

15. Scanlon, A., and Mikhailovsky, L., "Strength Evaluation of An Existing Concrete Bridge Based on Core and Non-Destructive Test Data," *Canadian Journal of Civil Engineering*, V. 14, No. 2, 1987, pp. 145-154. doi: 10.1139/l87-026

16. Koide, H.; Akita, H.; and Tomon, M., "Size Effect on Flexural Resistance Due to Bending Span of Concrete Beams." *Proceedings of the Third International Conference on Fracture Mechanics of Concrete Structures*, 1998, Freiburg, Germany, pp. 2121–2130.

17. VTAG, VecTor Analysis Group, Nonlinear Finite Element Analysis Software for Reinforced Concrete Structures, 2019, http://vectoranalysisgroup.com/.

18. Wong, P. S.; Vecchio, F. J.; and Trommels, H., "VecTor2 and FormWorks User's Manual," *Technical Report*, Department of Civil Engineering, University of Toronto, Toronto, ON, Canada, 2013, 318 pp.

19. Vecchio, F., and Collins, M., "The Modified Compression Field Theory for Reinforced Concrete Elements Subjected to Shear," *ACI Journal Proceedings*, V. 83, No. 2, Mar.-Apr. 1986, pp. 219-231.

20. Vecchio, F., "Disturbed Stress Field Model for Reinforced Concrete: Formulation," *Journal of Structural Engineering*, ASCE, V. 126, No. 9, 2000, pp. 1071-1077. doi: 10.1061/(ASCE)0733-9445(2000)126:9(1070)

21. Comite Euro-International Du Beton, "CEB—FIP Model Code for Concrete Structures," Brussels, Belgium, 1978.

22. Hunter, M. D.; Ferche, A. C.; and Vecchio, F. J., "Stochastic Finite Element Analysis of Shear-Critical Concrete Structures," *ACI Structural Journal*, accepted for publication..

APPENDIX

The Appendix contains additional material supporting the data and discussions contained in the journal article entitled “Influence of Spatial Variability of Concrete in Large Shear-Critical Structures.”

Appendix A: Competition results

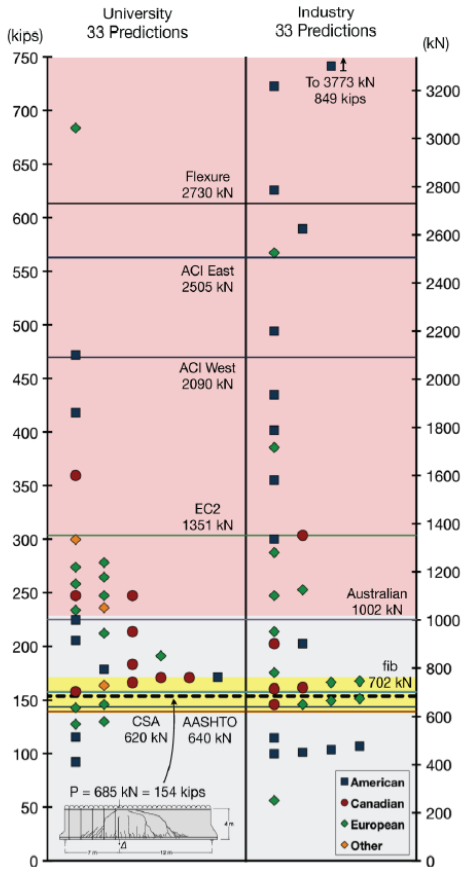

Fig. A – Comparison of predictions of failure point load with test result. (taken from Quach[2])

Appendix B: Slab strip thickness

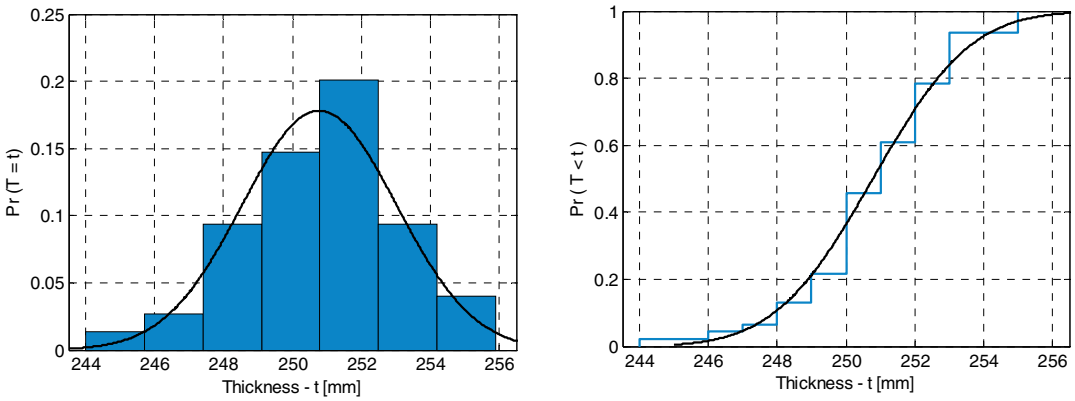

(a) *(b)*

Fig. B.1 – (a) Histogram and fitted PDF of thickness data. (b) Empirical and fitted CDF of thickness data.

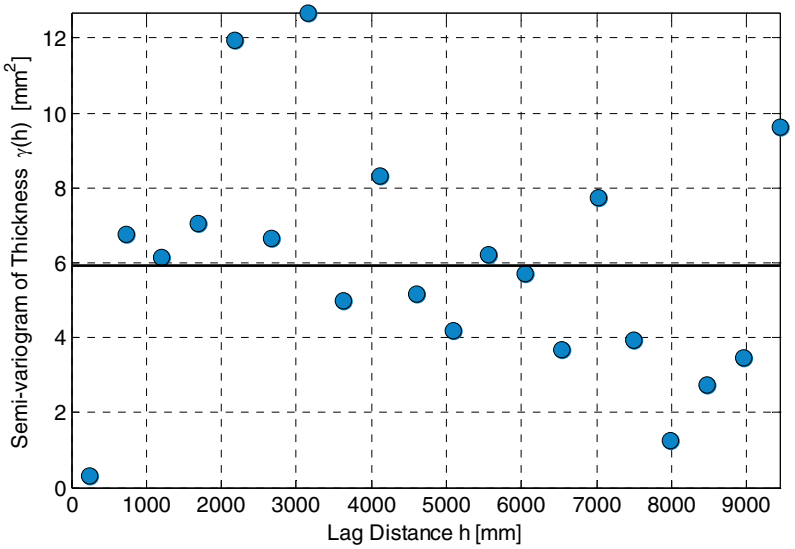

Fig. B.2 – Semivariogram of slab strip thickness. (Note 1 mm = 0.04 in.)

Appendix C: Concrete cylinder data analysis

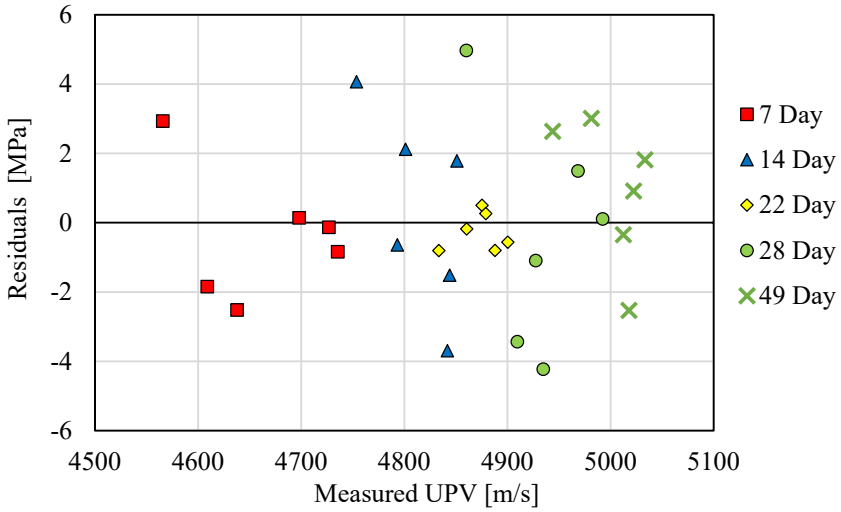

Fig. C.1 – Residuals from regression model. (Note: 1 MPa= 145 psi, 1 m/s=3.28 ft/s)

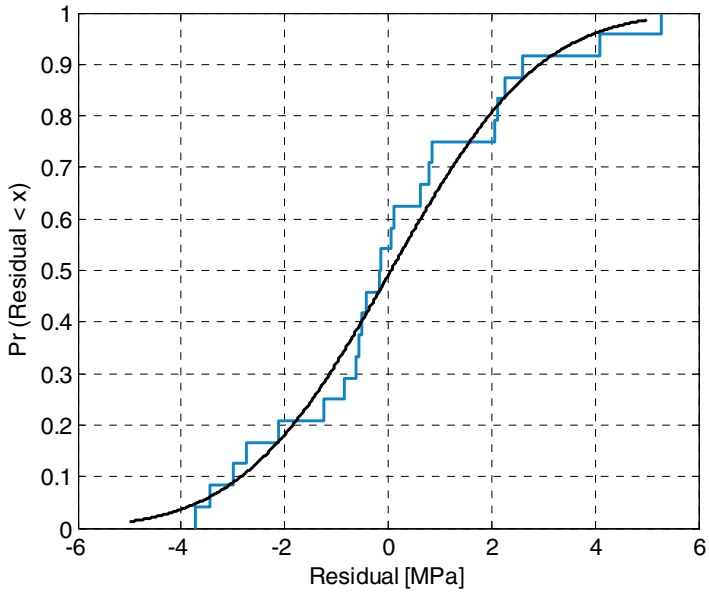

Fig. C.2 – Empirical cumulative distribution function and fitted distribution for residuals. (Note: 1 MPa= 145 psi)

Appendix D: PLS4000 UPV data analysis

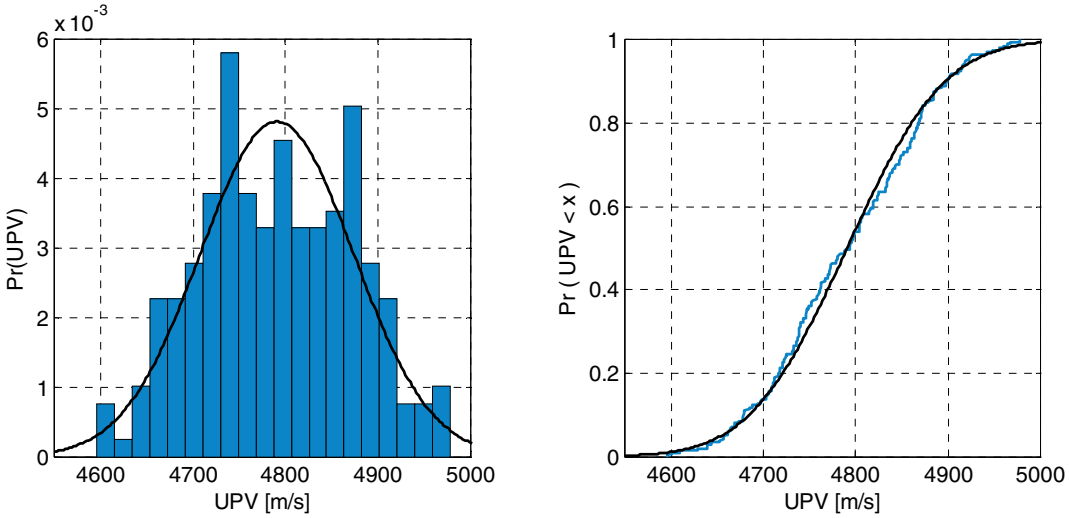

(a) *(b)*

Fig. D.1: Experimental UPV data and fitted distributions. (a) Histogram and PDF. (b) Empirical and fitted CDF. (Note: 1 m/s=3.28 ft/s)

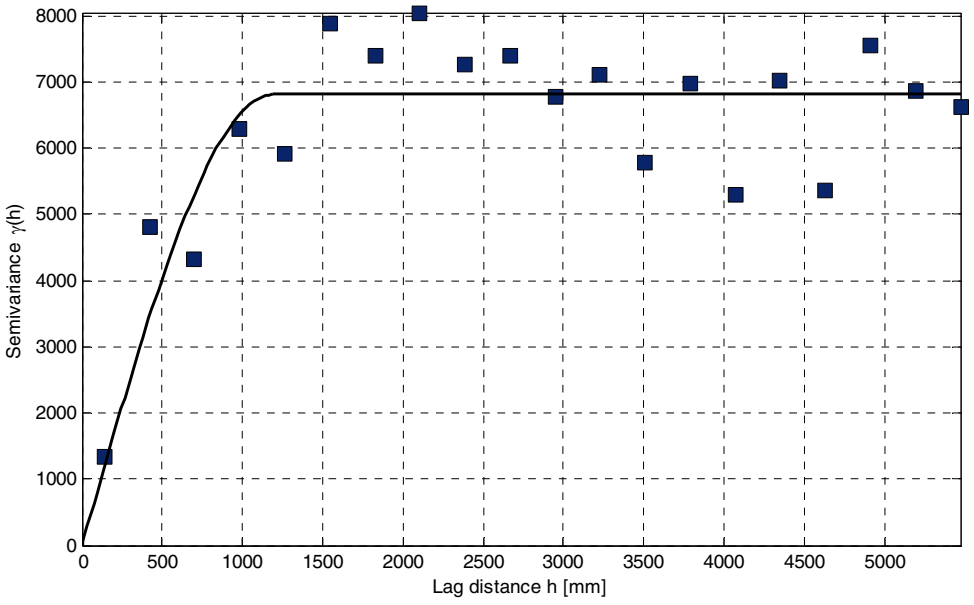

Fig. D.2: Fitted spherical semivariogram for experimental data.

Appendix E: Kriging maps calculation

Stein[11] presents a summary on how the kriging maps are calculated. The procedure described in this Appendix was used to produce kriging maps for the ultrasonic pulse velocity at the centre of each of the finite elements in the mesh.

The collected data were assumed to be part of a realization of a random field Z which takes the form shown in Eq. F1:

$$Z(x) = m(x)^T\beta + \varepsilon(x) \quad \text{(F1)}$$

where *m(x)* is the mean function, ε*(x)* is a random field with a mean of zero with a known covariance structure, and β is a vector of unknown coefficients. Kriging maps can be referred to as universal or ordinary. In the case of an ordinary kriging map, the parameter *m(x)* is assumed to be equal to 1.0 and thus the mean is an unknown constant. In the case of a universal kriging map, the mean function is variable with position. The spatial variation in the point loaded strip is assumed to be an ordinary kriging and thus the mean is constant. Kriging maps are also referred to as the best unbiased linear predictor. The best unbiased linear predictor assumes that the prediction $Z(x_0)$, for a vector of points, x_0, that lie between collected observations, can be represented by the form:

$$Z(x_0) = \lambda_0 + \lambda^T Z \quad \text{(F2)}$$

where $Z = \{Z(x_1), \dots, Z(x_n)\}$ is a set of observed values of the random field at points x_1 to x_n. This predictor is subject to two constraints:

$$E[\lambda_0 + \lambda^T Z] = E[Z(x_0)] \quad \text{(F3)}$$

$$\lambda_0 + \lambda^T M\beta = m(x)^T\beta \quad \text{(F4)}$$

where the measured values of the mean function x_1 to x_n is $M^T = \{m(x_1), \dots, m(x_n)\}$. Thus, it is concluded that:

$$\lambda_0 = 0 \quad \text{(F5)}$$

$$m(x_0) = M^T\lambda \quad \text{(F6)}$$

The solution of λ that solves this constrained minimization problem is then considered the best unbiased linear predictor for $Z(x_0)$, calculated as:

$$Z(x_0) = \lambda^T Z \quad \text{(F7)}$$

If a vector *v* is selected such that:

$$Z(x_0) = (\lambda + v)^T Z \quad \text{(F8)}$$

then it can be shown that:

$$m(x) = M^T(\lambda + v) = M^T\lambda + M^T v \quad \text{(F9)}$$

Because $m(x)=M^T\lambda$, it can be seen that $M^T v = 0$. In addition, Stein[11] shows that the best linear prediction for the weighting function is given by:

$$\lambda = K^{-1}k \quad \text{(F10)}$$

where $K = \text{cov}\{Z, Z^T\}$ and $k = \text{cov}\{Z, Z(x_0)\}$. Thus, if a vector μ is selected such that $M\mu = 0$, it follows that:

$$K\lambda - k = M\mu \quad \text{(F11)}$$

In matrix form these two conditions take the form:

$$\begin{bmatrix} K & M \\ M^T & O \end{bmatrix}\begin{bmatrix} \lambda \\ \mu \end{bmatrix} = \begin{bmatrix} k \\ m(x_0) \end{bmatrix} \quad \text{(F12)}$$

Where O is a matrix of zeros. This can be rearranged to:

$$\begin{bmatrix} \lambda \\ \mu \end{bmatrix} = \begin{bmatrix} K & M \\ M^T & O \end{bmatrix}^{-1}\begin{bmatrix} k \\ m(x_0) \end{bmatrix} \quad \text{(F13)}$$

Solving for λ yields:

$$\lambda = \{K^{-1} - K^{-1}M(M^TK^{-1}M)^{-1}M^TK^{-1}\}k + K^{-1}M(M^TK^{-1}M)^{-1}m(x_0) \quad \text{(F14)}$$

Thus, using the calculated data, unbiased estimates for values between collected data is estimated. However, the covariance values between the measured values Z and the locations of prediction $Z(x_0)$ need to be known. As such, the autocorrelation function calculated from the fitted semivariogram is used to produce the *k* matrix.

Appendix F: Stochastic analysis approach

Each stochastic simulation consisted of a random field using Latin hypercube sampling for the specified concrete strength, assumed to be 30 MPa (4350 psi). The stochastic analysis parameters for concrete are outlined in **Table F.1**. The steel properties were assumed to be deterministic.

Table F.1 – Stochastic simulation input properties for concrete

Variable	Model	Mean Value [MPa]	Standard Deviation [MPa]	Coefficient of Variation [%]
Compressive Strength $f_c' = 30\ MPa$	Bartlett and MacGregor[14]	38.57	7.14	18.6
Tensile Strength $f_t' = 1.81\ MPa$	Modified Mirza et al.[4]	1.81	0.23	12.7
Modulus of Elasticity $E_c = 25084\ MPa$	Modified Mirza et al.[4]	25084	2006.7	8.0

Note: 1 MPa = 145 psi.

The distributions from **Table F.1** are the global distributions. The spatial variation due to random fields for each simulation was based on the measured properties of PLS 4000 specimen. For a finite element simulation, each element can be assumed to take on a random value of a material property. However, it is rational to assume that a correlation exists between adjacent elements. To capture the spatial correlation between adjacent finite elements, the Gaussian random field was adopted. Random fields are spatially correlated stochastic samples which follow a specified distribution. Three parameters as required for generating a random field: the number of included eigenvalues, the random field variance, and the correlation length.

As discussed by Hunter[3], 80 eigenvalues are adequate in generating random fields for the correlation lengths typically observed in concrete. A correlation length of 1200 mm (47.2 in.) and a random field variance of 1.0. The random field is then scaled to meet the global distribution for concrete.